

Spectral signatures of many-body localization with interacting photons

P. Roushan^{1,*}, C. Neill^{2,*}, J. Tangpanitanon^{3,*}, V.M. Bastidas^{3,*}, A. Megrant¹, R. Barends¹, Y. Chen¹, Z. Chen², B. Chiaro², A. Dunsworth², A. Fowler¹, B. Foxen², M. Giustina¹, E. Jeffrey¹, J. Kelly¹, E. Lucero¹, J. Mutus¹, M. Neeley¹, C. Quintana², D. Sank¹, A. Vainsencher¹, J. Wenner², T. White¹, H. Neven¹, D. G. Angelakis^{3,4}, and J. Martinis^{1,2}

¹Google Inc., Santa Barbara, California, USA

²Department of Physics, University of California, Santa Barbara, California, USA

³Centre for Quantum Technologies, National University of Singapore, Singapore and

⁴School of Electrical and Computer Engineering, Technical University of Crete, Chania, Crete, Greece

Statistical mechanics is founded on the assumption that a system can reach thermal equilibrium, regardless of the starting state. Interactions between particles facilitate thermalization, but, can interacting systems always equilibrate regardless of parameter values? The energy spectrum of a system can answer this question and reveal the nature of the underlying phases. However, most experimental techniques only indirectly probe the many-body energy spectrum. Using a chain of nine superconducting qubits, we implement a novel technique for directly resolving the energy levels of interacting photons. We benchmark this method by capturing the intricate energy spectrum predicted for 2D electrons in a magnetic field, the Hofstadter butterfly. By increasing disorder, the spatial extent of energy eigenstates at the edge of the energy band shrink, suggesting the formation of a mobility edge. At strong disorder, the energy levels cease to repel one another and their statistics approaches a Poisson distribution - the hallmark of transition from the thermalized to the many-body localized phase. Our work introduces a new many-body spectroscopy technique to study quantum phases of matter.

Introduction. Consider a system of interacting particles isolated from the environment. Imagine it is initially prepared in a very low entropy state far from equilibrium. It is often observed that the system acts as its own thermal reservoir and approaches the equilibrium state. In this thermal phase the system shows ergodic behavior, where it uniformly explores all accessible states over time. Recent works discuss the emergence of another phase for the system in certain parameter regime where ergodicity breaks down and thermal equilibrium becomes unattainable [1–8]. This finding is rather surprising, since intuitively one may think that interacting systems are always able to thermalize themselves. This phase is referred to as the many-body localized (MBL) phase [9–16]. The conventional quantum phase transitions, e.g. from para- to ferro-magnetic, are characterized by changes in the groundstate of the system. However, the signatory differences between the thermalized and MBL phases are in dynamical behaviors, indicating that the transition involves change in the properties of all many-body eigenstates of the system. Hence the physics goes beyond the ground-state and requires study of the entire

energy spectrum, which constitutes an experimental challenge.

In classical physics, the characteristic (eigen) frequencies of the system and the shape of these vibrational modes are fundamental for understanding and designing mechanical structures and electrical circuits. Similarly, in quantum physics, the quantized eigen-energies and their associated wave-functions provides extensive information for predicting the chemistry of molecules or physics of condensed matter systems. Regardless of the underlying mechanism, creating local perturbations and recording the subsequent vibrational response of the system as a function of time can reveal the characteristic modes of that system. Our method for measuring the energy spectrum of a Hamiltonian is based on this and is extremely simple. For fixed Hamiltonians, the state of a system evolves according to Schrödinger equation

$$|\psi(t)\rangle = \sum_{\alpha} C_{\alpha} e^{-iE_{\alpha}t/\hbar} |\phi_{\alpha}\rangle, \quad (1)$$

where E_{α} is an eigen-energy of the Hamiltonian and $|\phi_{\alpha}\rangle$ is the corresponding eigenstate. Eqn. (1) implies that $\{E_{\alpha}\}$ and $\{C_{\alpha}\}$ determine the frequencies and the amplitudes of the modulations in $\psi(t)$, respectively. The similarity of Eqn. (1) and a Fourier transform (FT) relation suggests that the *frequencies* observed in the FT of the evolution could in principle reveal $\{E_{\alpha}\}$. In addition, the *magnitudes* of FT terms provide $\{C_{\alpha}\}$; these coefficients set the relative contribution of each $|\phi_{\alpha}\rangle$ to a given dynamics.

Using 9 superconducting qubits, we constructed a 1D bosonic lattice and implement a spectroscopy method based on the above-mentioned fundamental postulate of quantum mechanics. Each of our qubits can be thought of as a nonlinear oscillator. The Hamiltonian of the chain can be described by the Bose-Hubbard model

$$H_{BH} = \sum_{n=1}^9 \mu_n a_n^{\dagger} a_n + \frac{U}{2} \sum_{n=1}^9 a_n^{\dagger} a_n (a_n^{\dagger} a_n - 1) + J \sum_{n=1}^8 a_{n+1}^{\dagger} a_n + a_n^{\dagger} a_{n+1}, \quad (2)$$

where a^{\dagger} (a) denotes the bosonic creation (annihilation) operator, μ_n is the on-site potential, J is the hopping rate between nearest neighbour lattice sites, and U is the on-site interaction. The qubit frequency, the nearest neighbor coupling, and nonlinearity set μ_n , J , and U , respectively. In our system, we can vary the first two in ns time-scales, but

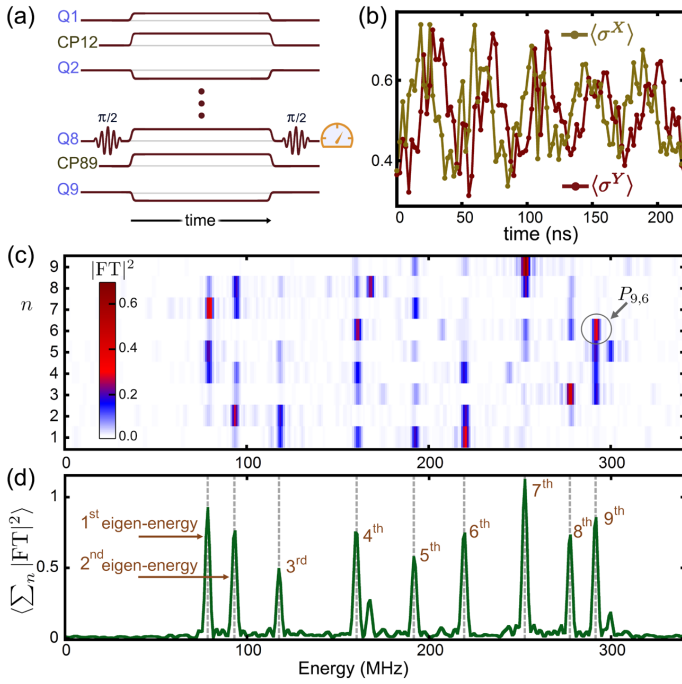


Figure 1. **Time-domain spectroscopy.** (a) Pulse sequence used to measure eigenvalues of a time-independent Hamiltonian, Eqn. (2) with $J/2\pi = 50$ MHz, $U = 0$, and $\mu_n/2\pi$ randomly chosen from $[0, 100]$ MHz. Initially, all the qubits are in the $|0\rangle$ state. Using a microwave pulse, one of the qubits is then placed on the superposition of $|0\rangle$ and $|1\rangle$ state ($Q8$ depicted here). The coefficients in the Hamiltonian are set by applying square pulses on the qubits $\{Q_n\}$ and couplers $\{CP\}$. After the evolution, a microwave $\pi/2$ pulse is applied to the qubit in order to measure $\langle \sigma_n^X \rangle$ or $\langle \sigma_n^Y \rangle$. (b) Typical dataset showing $\langle \sigma_n^X \rangle$ and $\langle \sigma_n^Y \rangle$ versus time. (c) The FT of $\chi_1(n) = \langle \sigma_n^X \rangle + i\langle \sigma_n^Y \rangle$ for $n \in \{1, 2, \dots, 9\}$. The peaks in the FT correspond to the eigenvalues of the Hamiltonian. The probability of a Fock state on $Q6$ to be in the 9th eigenstate $P_{9,6}$ is highlighted. (d) Average of the FT amplitudes shown in (c). Averaging is done to show all 9 peaks in one curve.

U is fixed.

In Fig. 1 we show how to identify the eigen-energies of Eqn. (2) when it describes hopping of a single photon in a disordered potential. In the beginning of the sequence there is no photon in the system and all the qubits are in $|0\rangle$ state. Then, we place the n^{th} qubit Q_n in the superposition of $|0\rangle$ and $|1\rangle$ state (Fig. 1(a)). We measure the evolution of $\langle \sigma_n^X \rangle$ and $\langle \sigma_n^Y \rangle$, where σ^X and σ^Y are Pauli operators (acting on the $|0\rangle$ and $|1\rangle$ sub-space) (Fig. 1(b)). From the $\langle \sigma_n^X \rangle$ and $\langle \sigma_n^Y \rangle$ measurements we construct $\chi_1(n) \equiv \langle \sigma_n^X \rangle + i\langle \sigma_n^Y \rangle$. Next, we vary n from 1 to 9 to assure that the energy spectrum is fully resolved. By varying n the initial states form a complete basis, and then every energy eigen-state is certain to have some overlap with one of the initial states and hence can be detected. Fig. 1(c) shows the FTs of $\chi_1(n)$ for each Q_n in which distinct peaks can be readily identified. The result of averaging the FTs is depicted in Fig. 1(d), where 9 peaks appear and their frequencies are the 9 eigen-energies of the Hamiltonian. The particular choices of initial

states and the observables are made to avoid appearance of undesired energy peaks in the spectrum [17].

Simulating 2D electrons. Next, we demonstrate our capability to accurately set the terms in a specific Hamiltonian and resolve the corresponding eigen-energies. We simulate the problem of Bloch electrons on a 2D lattice subject to a perpendicularly applied magnetic field B [18–24]. The magnetic length ($l_B = \sqrt{\hbar/eB}$) and lattice constant a characterize the electron’s motion, and their interplay sets the physics. The resulting energy spectrum was first calculated by Hofstadter and resembles a butterfly [18]. For typical crystals, the magnetic field required to ‘squeeze’ one flux quantum through the unit cell is of the order of several tens of thousands of Tesla, too high to be experimentally feasible.

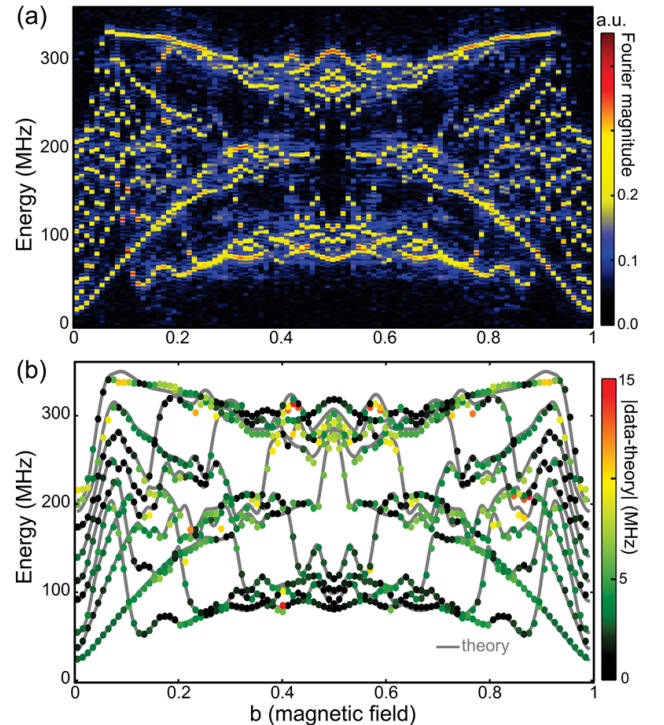


Figure 2. **Hofstadter butterfly.** In Eq. (3), we set on-site potentials $\Delta/2\pi = 50$ MHz and coupling $J/2\pi = 50$ MHz. (a) Data similar to Fig. 1(d) is shown for 100 values of dimensionless magnetic field b ranging from 0 to 1. (b) For each b value, we identify 9 peaks and plot their location as a colored dot. The numerically computed eigenvalues of Eq. (2) are shown with gray lines. The color of each dot is the difference between the measured eigenvalue and the numerically computed one.

The Hofstadter energy spectra can be parameterized by a single dimensionless magnetic field $b = a^2 eB/\hbar$ which counts the number of magnetic flux quanta per unit cell. In the tight binding approximation the Schrödinger equation takes the form of 1D Harper Hamiltonian [18]

$$H_{\text{Harper}} = \Delta \sum_{n=1}^9 \cos(2\pi nb) a_n^\dagger a_n + J \sum_{n=1}^8 a_{n+1}^\dagger a_n + a_n^\dagger a_{n+1}. \quad (3)$$

The H_{Harper} is the special case of H_{BH} , reached by setting $\mu_n = \Delta \cos(2\pi nb)$ and exciting only one photon in the sys-

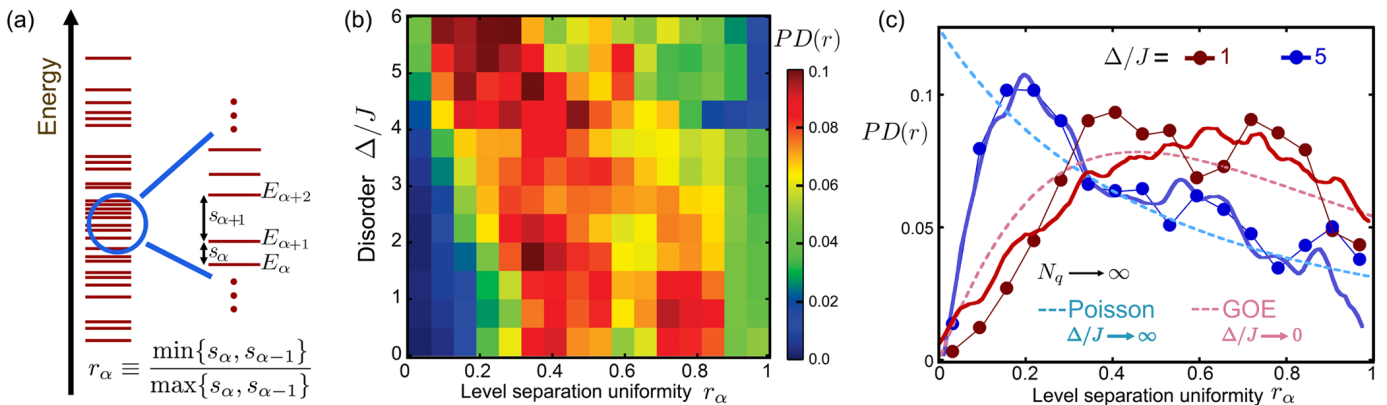


Figure 3. **Level statistics and transition from GOE to Poisson.** In Eqn. (2), we set hopping to $J/2\pi = 50$ MHz which fixes $U/J = 3.5$. In total, 4 different irrational values of $b \in [0, 1]$ are chosen and the results are averaged. (a) The schematic of energy levels shows how r_α is defined. (b) The measured histogram of $P(r)$ measured for various Δ/J values is presented in color. (c) The measured histogram $P(r)$ of $\{r_\alpha\}$ for $\Delta/J = 1$ and 5. The dashed lines are plots of P_{Poisson} and P_{GOE} according to Eqn. (5), and the solid lines are numerical simulations. The change from GOE toward Poisson is indicative of vanishing of level repulsion when Δ becomes larger.

tem, i.e. $U = 0$. Note that in this limit the fermionic or bosonic nature of the particle does not matter. In Fig. 2, we vary b from 0 to 1 and realize 100 different H_{Harper} . Similar to Fig. 1, for each b value, initial states with n^{th} qubit excited are created and the evolution of $\langle \sigma_n^X \rangle$ and $\langle \sigma_n^Y \rangle$ are measured, and n is varied from 1 to 9. For each b value, Fig. 2(a) shows the magnitude summation of the FT of $\{\chi_1(n)\}$.

For large lattices with many energy levels, it is theoretically known that for rational b all energy bands split into sub-bands, and for irrational b the spectra become fractal and form a Cantor set. Since we have only 9 levels, what we see in Fig. 2(a) are the remnants of those bands. Nevertheless, the overall measured spectrum still resembles a butterfly. We focus on this featureful pattern of level crossings and meanderings and ask how well the measurements match simulation. In Fig. 2(b), we present the numerically computed eigen-energies with solid gray lines and the measured peaks in (a) with colored dots. The color of the dots shows the distance in MHz of the peaks from the simulation values. The average deviation is 3.5 MHz. This implies we can set the matrix elements of the Hamiltonian, which in this case includes 17 terms, with $< 2\%$ error. This unprecedented capability in controlling a large quantum system is achieved through careful modeling of the qubits as non-linear resonators.

By placing two photons in the system, we next study the simplest interacting cases ($U \neq 0$). The rest of data presented in this work is taken by using the following procedure (2-photon protocol). We realize a quasi-periodic potential by setting $\mu_n = \Delta \cos(2\pi nb)$. In total, 4 different irrational values of $b \in [0, 1]$ are chosen and the corresponding results are averaged. The irrational choice of b assures that the periodicity of the potential and lattice are incommensurate. In Eqn. (2), we set $J/2\pi = 50$ MHz, which results in $U/J = 3.5$. The initial states are made by placing two

qubits (Qn and Qm) in the superposition of the $|0\rangle$ and $|1\rangle$ states. We measure two-point correlations and construct $\chi_2(n, m) \equiv \langle \sigma_n^X \sigma_m^X \rangle - \langle \sigma_n^Y \sigma_m^Y \rangle + i \langle \sigma_n^X \sigma_m^Y \rangle + i \langle \sigma_n^Y \sigma_m^X \rangle$. The peaks observed in the FT of $\chi_2(n, m)$ are the eigen-energies of H_{BH} in the two-photon manifold [17].

Energy level statistics in an interacting system.

Perhaps the most direct way of examining ergodic dynamics and its breakdown is by studying the distribution of the energy levels [25–27]. Using the 2-photon protocol, we measure the evolution of $\chi_2(n, m)$ for various strengths of disorder Δ . We identify the peaks in the FT of $\chi_2(n, m)$ as the energy levels E_α . Let $s_\alpha = E_{\alpha+1} - E_\alpha$ be the nearest-neighbor spacings (illustrated Fig. 3(a)), and level separation uniformity $r_\alpha \equiv \min\{s_\alpha, s_{\alpha-1}\} / \max\{s_\alpha, s_{\alpha-1}\}$. From our measured $\{E_\alpha\}$ we compute the associated $\{r_\alpha\}$ and construct their probability distribution (PD , Fig. 3(b)). For low disorder, the PD is mainly centered around the r_α values close to half, and with increase of disorder the histogram's peak shifts toward smaller r_α values.

It has been postulated that in the ergodic phase the statistics of levels is the same as the ensemble of real Hermitian random matrices, which follow the Gaussian Orthogonal ensemble (GOE) [27]. In the localized phase, the energy levels become uncorrelated due to disorder and hence it is expected to show a Poisson distribution in energy landscape. The probability distribution of $\{r_\alpha\}$ for the ergodic and many-body localized phases, respectively, are

$$PD_{\text{GOE}}(r) = \frac{27}{4} \frac{r + r^2}{(1 + r + r^2)^{5/2}}, PD_{\text{Poisson}}(r) = \frac{2}{(1 + r)^2}. \quad (4)$$

In Fig. 3(c), we focus on $\Delta/J = 1$ and 5, showing the measured histograms with dots and the numerical simulations with solid lines. The dashed lines are plots of Eqn. (5), providing the expected behavior in the thermodynamic limit (number of sites $N_q \rightarrow \infty$), and for limiting values of Δ/J . In contrast to these cases, the finite size of our chain results

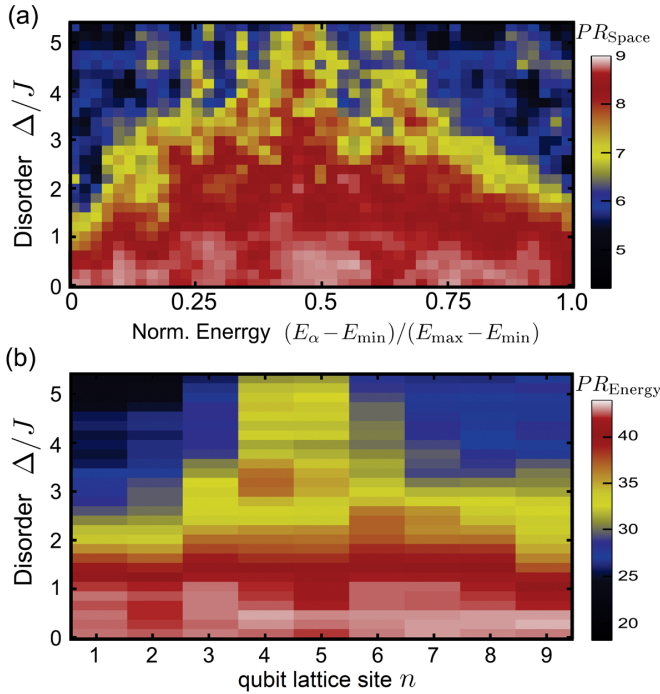


Figure 4. **Participation ratio and Mobility edges.** In Eqn. (2), we set $b = (\sqrt{5} - 1)/2$, $J/2\pi = 50$ MHz, which results in $U/J = 3.5$. We measure the evolution of $\chi_2(n, m) = \langle \sigma_n^X \sigma_m^X \rangle + \langle \sigma_n^Y \sigma_m^Y \rangle + i \langle \sigma_n^X \sigma_m^Y \rangle + i \langle \sigma_n^Y \sigma_m^X \rangle$ for all pairs of $n, m \in \{1, 2, \dots, 9\}$ as a function time for various strengths of disorder Δ . From the magnitude of the peaks seen in the FT of the data the probabilities relating the positions of two-photon Fock states to energy eigenstates $\{P_{\alpha,n}\}$ are extracted. See [17] for details. The computed (a) PR_{Space} and (b) PR_{Energy} based on Eqn. (4) are plotted. The $E_{\max} - E_{\min}$ is the width of the energy band at a given Δ .

in features that can be seen in both data and simulation. When disorder is small, the energy eigenstates are extended across the chain (we will show this in Fig. 4,) and hence the energy levels repel each other. Consequently, there are strong correlations between the levels and an equidistant distribution of levels would be favorable. When Δ becomes larger, the eigenstates become localized in space and unaware of each others presence at a given energy and level repulsion ceases. Therefore, the levels independently distribute themselves, showing a Poisson distribution in the energy landscape. The exact realization of Poisson distribution takes place only when $J/\Delta \rightarrow 0$; in our case $J/\Delta = 0.2$, which is where the peak in the histogram appears. Since the Poisson distribution is the signature of independent events, we conclude that the transition from ergodic to localized phase is associated with vanishing correlations in energy levels.

Spatial extend of eigen-energies. A key signature of transition from ergodic to MBL phase is the change in the localization length of the system from being extended over entire system to localized over a few lattice sites. This physics can be studied by measuring the probability of each energy eigen-state being present at each lattice site $\{P_{\alpha,n}\}$ [17].

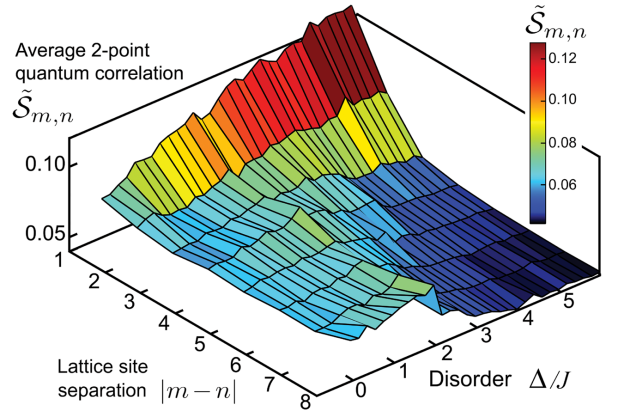


Figure 5. **Quantum correlations.** In Eqn. (2), we set $b = (\sqrt{5} - 1)/2$, $J/2\pi = 50$ MHz, and $U/2\pi = 175$ MHz. We measure $\tilde{S}_{m,n} = |\langle \sigma_m^1 \sigma_n^2 \rangle - \langle \sigma_m^1 \rangle \langle \sigma_n^2 \rangle|$ as a function time for various strengths of disorder Δ , where $\sigma^1, \sigma^2 \in \{\sigma^X, \sigma^Y\}$ and $m, n \in \{1, 2, \dots, 9\}$. All $\binom{9}{2} = 36$ possible pairs of qubits are excited. The color shows $\tilde{S}_{m,n}$ averaged over time (from 0 to 250 ns) and combinations with the same $|m-n|$. The change of correlations from almost uniform to exponentially decaying is consistent with change in behavior from ergodic to localized.

In our method, the frequencies of the FT signal give the eigen-energies, and from the magnitude of the FT terms $\{P_{\alpha,n}\}$ can be measured. For instance, $P_{9,6}$ is highlighted in Fig. 1(c). In the study of metal-insulator transition [28?], a common way to quantify the extension in real-space or energy landscape is via the second moment of the probabilities, defined by Participation Ratio (PR)

$$PR_{\text{Space}}(\alpha) \equiv 1 / \sum_n P_{\alpha,n}^2, \quad PR_{\text{Energy}}(n) \equiv 1 / \sum_\alpha P_{\alpha,n}^2. \quad (5)$$

PR_{Space} indicates the number of sites over which an energy eigenstate $|\phi_\alpha\rangle$ has an appreciable magnitude. Similarly, PR_{Energy} measures how many energy eigenstates have significant presence on lattice site n . Note that the first moment of the probability distributions is normalization conditions $\sum_\alpha P_{\alpha,n} = 1$ and $\sum_n P_{\alpha,n} = 1$.

Demonstrated that we can fully resolved the energy spectrum of the two-photon energy manifold, we now extract $\{P_{\alpha,n}\}$. In Fig. 4(a), we compute PR_{Space} for various disorder strengths and present them in the order of increasing energy. In this energy manifold, there are 36 single (e.g. $|001000100\rangle$) and 9 double occupancy states (e.g. $|000020000\rangle$), which gives $\binom{9}{2} + \binom{9}{1} = 45$ energy levels. For low disorder ($\Delta/J < 1$), PR_{Space} is about 8, indicating almost all energy eigenstates are extended over the entire chain of 9 qubit lattice sites. As the strength of disorder increases, the eigenstates with their energies close to the edge of the energy band start to shrink, while eigenstates with energies in the middle of the band remain extended at larger disorders. This is consistent with the notion that localization begins at the edges of the band, and a mobility edge forms (the yellow hue) and approaches the center of the band as disorder becomes stronger [28]. In Fig. 4(b), we plot the PR_{Energy} , which shows that as the disorder be-

comes stronger, the number of eigenstates present at a given lattice site reduces, indicating that eigenstates are becoming localized on lattice sites. Furthermore, with increasing disorder, the eigenstates are avoiding the edges of the chain and more eigenstates have presence toward the center of the chain. The changes in PR_{Space} and PR_{Energy} are the fastest near $\Delta/J = 2$, suggestive of a phase transition that has been smeared out due to finite size effects. Nevertheless, we emphasize that the quantum phase transition to the MBL phase is only defined in the thermodynamic limit ($N_q \rightarrow \infty$) [15]. Given the finite size of our system and the presence of only two interacting particles, it is interesting that we see several signatures associated with the MBL phase transition.

Quantum correlations. To provide a comprehensive picture of the transition to the localized phase, we study two-site quantum correlations $\mathcal{S}_{m,n}$ as a function of disorder strength Δ and distance between lattice sites $|m - n|$. We measure $\mathcal{S}_{m,n} \equiv |\langle \sigma_m^1 \sigma_n^2 \rangle - \langle \sigma_m^1 \rangle \langle \sigma_n^2 \rangle|$, where $\sigma^1, \sigma^2 \in \{\sigma^X, \sigma^Y\}$ and $m, n \in \{1, 2, \dots, 9\}$, for all m and n combinations and Pauli operators. Fig. 5(a) shows $\tilde{\mathcal{S}}_{m,n}$, computed by averaging $\mathcal{S}_{m,n}$ over time and all possible combinations with the same $|m - n|$. For Δ up to $\Delta/J \approx 2$, $\tilde{\mathcal{S}}_{m,n}$ is rather symmetric in $|m - n|$, and for $\Delta/J > 2$ it exponentially decays with $|m - n|$. Intuitively, strong Δ creates large potential barriers that wave-functions cannot tunnel through and consequently correlations cannot develop. Interestingly, for $|m - n| < 3$, as disorder becomes stronger, $\tilde{\mathcal{S}}_{m,n}$ becomes larger, indicating that correlations cannot propagate far and locally build up in the potential 'puddles'. These observations are consistent with the signatures of the transitions from the metallic phase, where correlations are distance independent, to the localized phase where they decay rapidly with distance.

Conclusion. Our work demonstrates the novel information about various phases that can be extracted if one directly resolves the energy levels of a system. Our findings signify the generality of the MBL phenomena and the fact that its underlying physics prevails regardless of the details of the system.

Acknowledgments: We acknowledge discussions with Y. Bahri, D. Huse, E. Kapit, M. Knap, L. Hormozi, O. Kyriienko, M. F. Maghrebi, V. Oganesyan, A. Scardicchio, and G. Zhu.

Author Contributions: P.R. and C.N. performed the experiment. J.T., V.M.B., and D. G. A. provided theoretical assistance. P.R., C.N., J.T., V.M.B., and D.G.A. analysed the data and co-wrote the manuscript. All of the UCSB and Google team members contributed to the experimental setup.

* These authors contributed equally to this work.

- [1] D.M. Basko, I.L. Aleiner, and B.L. Altshuler, "Metal-insulator transition in a weakly interacting many-electron system with localized single-particle states," *Annals of Physics* **321**, 1126–1205 (2006).
- [2] R. Nandkishore and D. A. Huse, "Many-body localization and thermalization in quantum statistical mechanics," *Annual Review of Condensed Matter Physics* **6**, 15–38 (2015).
- [3] E. Altman and R. Vosk, "Universal dynamics and renormalization in

- many-body-localized systems," *Annual Review of Condensed Matter Physics* **6**, 383 (2015).
- [4] N. Y. Yao, C. R. Laumann, S. Gopalakrishnan, M. Knap, M. Muller, E. A. Demler, and M. D. Lukin, "Many-body localization in dipolar systems," *Phys. Rev. Lett.* **113**, 243002 (2014).
- [5] M. Schreiber, S. S. Hodgman, P. Bordia, H. P. Luschen, M. H. Fischer, R. Vosk, E. Altman, U. Schneider, and I. Bloch, "Observation of many-body localization of interacting fermions in a quasirandom optical lattice," *Science*, 842–845 (2015).
- [6] J. Smith, A. Lee, P. Richerme, B. Neyenhuis, P. W. Hess, P. Hauke, M. Heyl, D. A. Huse, and C. Monroe, "Many-body localization in a quantum simulator with programmable random disorder," *Nature Physics* **12** (2016).
- [7] A. M. Kaufman, M. E. Tai, A. Lukin, M. Rispoli, R. Schittko, P. M. Preiss, and M. Greiner, "Quantum thermalization through entanglement in an isolated many-body system," *Science* **353**, 794–800 (2016).
- [8] J. Choi, S. Hild, J. Zeiher, P. Schauss, T. Yefsah A. Rubio-Abadal, V. Khemani, D. A. Huse, I. Bloch, and C. Gross, "Exploring the many-body localization transition in two dimensions," *Science* **352**, 1547–1552 (2016).
- [9] A. Pal and D. A. Huse, "Many-body localization phase transition," *Phys. Rev. B* **82**, 174411 (2010).
- [10] A. Chandran, V. Khemani, C. R. Laumann, and S. L. Sondhi, "Many-body localization and symmetry-protected topological order," *Phys. Rev. B* **89**, 144201 (2014).
- [11] M. Serbyn, M. Knap, S. Gopalakrishnan, Z. Papic, N. Y. Yao, C. R. Laumann, D. A. Abanin, M. D. Lukin, and E. A. Demler, "Interferometric probes of many-body localization," *Phys. Rev. Lett.* **113**, 147204 (2014).
- [12] J. A. Kjall, J. H. Bardarson, and F. Pollmann, "Many-body localization in a disordered quantum ising chain," *Phys. Rev. Lett.* **113**, 107204 (2014).
- [13] M. Serbyn, Z. Papic, and D.A. Abanin, "Criterion for many-body localization-delocalization phase transition," *Phys. Rev. X* **5**, 041047 (2015).
- [14] Y. Bahri, R. Vosk, E. Altman, and A. Vishwanath, "Localization and topology protected quantum coherence at the edge of hot matter," *Nature Communications* **6**, 7341 (2015).
- [15] John Z. Imbrie, "Diagonalization and many-body localization for a disordered quantum spin chain," *Phys. Rev. Lett.* **117**, 027201 (2016).
- [16] F. Iemini, A. Russomanno, D. Rossini, A. Scardicchio, and R. Fazio, "Signatures of many-body localization in the dynamics of two-site entanglement," *Phys. Rev. B* **94**, 214206 (2016).
- [17] See supplementary material.
- [18] Douglas R. Hofstadter, "Energy levels and wave functions of bloch electrons in rational and irrational magnetic fields," *Phys. Rev. B* **14**, 2239–2249 (1976).
- [19] D. Jaksch and P. Zoller, "Creation of effective magnetic fields in optical lattices: the hofstadter butterfly for cold neutral atoms," *New Journal of Physics* **5** (2003).
- [20] L. A. Ponomarenko, R. V. Gorbachev, G. L. Yu, D. C. Elias, R. Jalil, A.A. Patel, A. Mishchenko, A. S. Mayorov, C. R. Woods, J. R. Wallbank, M. Mucha-Kruczynski, B. A. Piot, M. Potemski, I. V. Grigorieva, K. S. Novoselov, F. Guinea, V. I. Fal'ko, and A. K. Geim, "Cloning of dirac fermions in graphene superlattices," *Nature* **497**, 594–597 (2013).
- [21] C. R. Dean, L. Wang, P. Maher, C. Forsythe, F. Ghahari, Y. Gao, J. Katoch, M. Ishigami, P. Moon, M. Koshino, T. Taniguchi, K. Watanabe, K. L. Shepard, J. Hone, and P. Kim, "Hofstadter's butterfly and the fractal quantum hall effect in moire superlattices," *Nature* **497**, 598–1430 (2013).
- [22] B. Hunt, J. D. Sanchez-Yamagishi, A. F. Young, M. Yankowitz, B. J. LeRoy, K. Watanabe, T. Taniguchi, P. Moon, M. Koshino, P. Jarillo-Herrero, and R. C. Ashoori, "Massive dirac fermions and hofstadter butterfly in a van der waals heterostructure," *Science* **340**, 1427–602 (2013).
- [23] H. Miyake, G. A. Siviloglou, C. J. Kennedy, W. Burton, and W. Ketterle, "Realizing the harper hamiltonian with laser-assisted tunneling in optical lattices," *Phys. Rev. Lett.* **111**, 185302 (2013).
- [24] M. Aidelsburger, M. Atala, M. Lohse, J. T. Barreiro, B. Paredes, and I. Bloch, "Realization of the hofstadter hamiltonian with ultracold atoms in optical lattices," *Phys. Rev. Lett.* **111**, 185301 (2013).
- [25] Vadim Oganesyan and David A. Huse, "Localization of interacting fermions at high temperature," *Phys. Rev. B* **75**, 155111 (2007).
- [26] Y. Y. Atas, E. Bogomolny, O. Giraud, and G. Roux, "Distribution of the ratio of consecutive level spacings in random matrix ensembles," *Phys. Rev. Lett.* **110**, 084101 (2013).
- [27] O. Bohigas, M. J. Giannoni, and C. Schmit, "Characterization of chaotic quantum spectra and universality of level fluctuation laws," *Phys. Rev. Lett.* **52**, 1–4 (1984).
- [28] E. Abrahams, "50 years of anderson localization," (2010).

Supplementary materials: Spectral signatures of many-body localization with interacting photons

P. Roushan^{1,*}, C. Neill^{2,*}, J. Tangpanitanon^{3,*}, V.M. Bastidas^{3,*}, A. Megrant¹, R. Barends¹, Y. Chen¹, Z. Chen², B. Chiaro², A. Dunsworth², A. Fowler¹, B. Foxen², E. Jeffrey¹, J. Kelly¹, E. Lucero¹, J. Mutus¹, M. Neeley¹, C. Quintana², D. Sank¹, A. Vainsencher¹, J. Wenner², T. White¹, H. Neven¹, D. G. Angelakis^{3,4}, and J. Martinis^{1,2†}

¹Google Inc., Santa Barbara, CA 93117, USA

²Department of Physics, University of California, Santa Barbara, CA 93106, USA

³Centre for Quantum Technologies, National University of Singapore, 2 Science Drive 3, 117542, Singapore and

⁴School of Electrical and Computer Engineering, Technical University of Crete, Chania, Crete, 73100 Greece

CONTENTS

1. Device: the superconducting qubits with gmon architecture	1
2. Spectroscopy based on fundamental postulate of quantum mechanics	2
2.1 Energy differences vs. absolute energies	2
2.2 Single-particle spectroscopy: generalization	3
2.3 Two-particle spectroscopy: generalization	3
2.4 Computation of the Participation Ratio	5
2.5 Resolving the spectrum for large Hilbert-spaces	6
3. Two-point quantum correlations	7
4. Hamiltonians used in this work	8
4.1 Mapping the 2D quantum Hall model to the 1D Harper model	8
4.2 Aubry-Andre model	8
References	9
1. DEVICE: THE SUPERCONDUCTING QUBITS WITH GMON ARCHITECTURE	

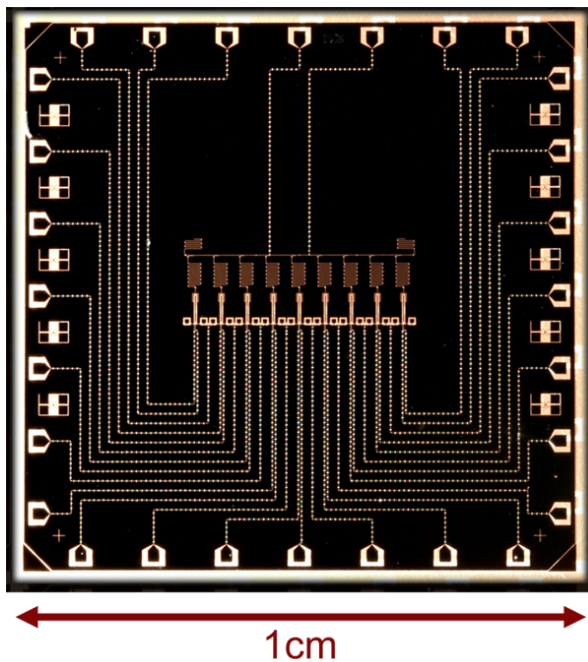


Figure S1. An optical micrograph of the device which consists of 9 qubits in a 1D chain with adjustable coupling between every pair of qubits. The qubits appear as small vertical rectangles in the middle of the chip. The couplers are the two square loops that are between the qubits. The wiring lines that are routed to the perimeter of the chip are used to control the qubits and the interaction between them. The meandering lines above the qubits are the readout resonators. The qubits are connected with an adjustable coupler. Each qubit is a non-linear LC resonator, and the two qubits are inductively coupled through the mutual inductance to a coupler loop. The coupler loop has a single Josephson junction, which can be tuned by applying magnetic flux into the coupler loop, allowing variable coupling strength between the two qubits in a few ns time scales. For a detailed discussion of principle of operation and calibration routines, see references [1–4].

2. SPECTROSCOPY BASED ON FUNDAMENTAL POSTULATE OF QUANTUM MECHANICS

According to the time-independent Schrödinger equation, the time evolution of the state of the system $|\psi(t)\rangle$ is given

$$|\psi(t)\rangle = \sum_{\alpha} C_{\alpha} e^{-iE_{\alpha}t} |\phi_{\alpha}\rangle, \quad (1)$$

where $C_{\alpha} = \langle \phi_{\alpha} | \psi_0 \rangle$, and $|\psi_0\rangle$ is the initial state. On the other hand, an observable in the energy basis can be written as

$$\hat{O} = \sum_{\alpha, \alpha'} O_{\alpha', \alpha} |\phi_{\alpha'}\rangle \langle \phi_{\alpha}|, \quad (2)$$

where $O_{\alpha', \alpha} = \langle \phi_{\alpha'} | \hat{O} | \phi_{\alpha} \rangle$ and accordingly its expectation value is:

$$O(t) = \langle \psi(t) | \hat{O} | \psi(t) \rangle = \sum_{\alpha, \alpha'} O_{\alpha', \alpha} C_{\alpha} C_{\alpha'}^* e^{-i(E_{\alpha} - E_{\alpha'})t}. \quad (3)$$

For our spectroscopy purpose, we are interested in energies E_{α} and not energy differences $E_{\alpha} - E_{\alpha'}$. The above relation suggests that when measuring any observable one will generally end up with energy differences. It is not obvious *a priori* how to avoid energy differences. However, proper choices of observables and initial states can help to overcome this issue, enabling extraction of eigen-energies. A key observation here is that one should somehow fix $E_{\alpha'}$ to a specific energy, i.e., a reference energy. See the schematic in Fig. S2.

2.1 Energy differences vs. absolute energies

We illustrate the method by considering first a simple example of two coupled harmonic oscillators described by the tight-binding Hamiltonian

$$H_{\text{dimer}} = \omega(a_1^{\dagger}a_1 + a_2^{\dagger}a_2) - J(a_1^{\dagger}a_2 + H.c.), \quad (4)$$

where ω is the frequency of the oscillators, J is the hopping rate, a_1 and a_2 are bosonic annihilation operators acting on the first and the second oscillators, respectively. The single-photon eigenstates are $|\phi_{\pm}\rangle = (|10\rangle \pm |01\rangle)/\sqrt{2}$ with the eigen-energies $E_{\pm} = \omega \pm J$, where $|10\rangle = a_1^{\dagger}|00\rangle$, $|01\rangle = a_2^{\dagger}|00\rangle$ and $|00\rangle$ is the vacuum. Different choices of initial states and observables are shown in Fig. S2 (right panel). One quickly realizes that $a^{\dagger}a$ would have energy differences and not suitable; but a might, if the proper initial state is chosen. A proper initial state would be the superposition of the relevant number state (here the $|10\rangle$ state) that has one particle and the vacuum $|00\rangle$. The vacuum here serves as the appropriate reference state and has energy $E_{\alpha'} = 0$. Since a is non-Hermitian and hence not an observable, a cannot be measured directly. However, it can be easily inferred from its Hermitian "quadratures" σ^X and σ^Y as $\langle a \rangle = \langle \sigma^X \rangle + i\langle \sigma^Y \rangle$, where $\sigma^X = |1\rangle\langle 0| + |0\rangle\langle 1|$ and $\sigma^Y = i|1\rangle\langle 0| - i|0\rangle\langle 1|$ are Hermitian and hence observable.

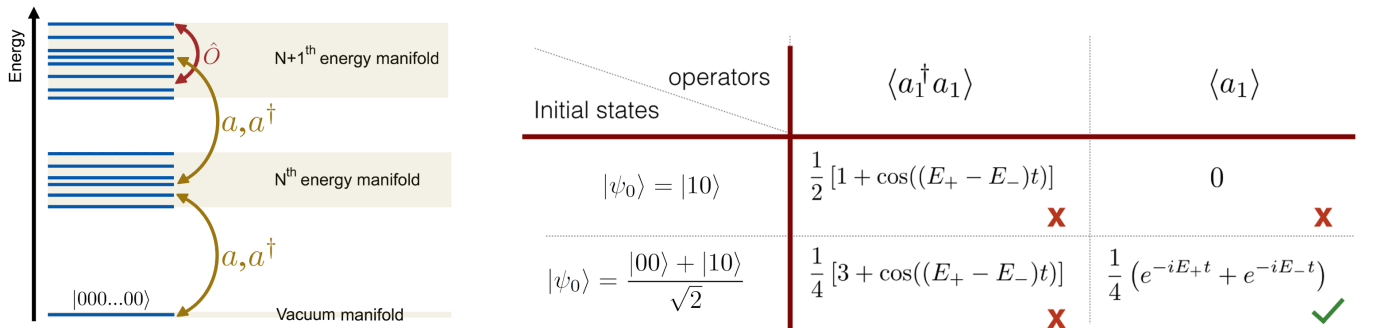


Figure S2. (a) The schematic shows that generally operators, such as \hat{O} connect different levels, and hence in their observables one would see the energy differences of the levels. The raising a^{\dagger} and lowering a operators connect states in different manifolds. It is a fortunate coincidence that there is a manifold with only one state in it, the vacuum manifold, which can act as a energy reference. The initial states that are superposition of vacuum state and some other state are necessary for having a functional protocol. (b) We show expectation values of different operators for two different initial states, associated with the example that we used. Note that both proper initial states and choice of operators are needed to have a useful protocol.

2.2 Single-particle spectroscopy: generalization

Now let us consider a general particle-conserving interacting Hamiltonian H in a lattice and assume first that there is only one particle in the system. As before, we choose an initial state as a product state of the form

$$|\psi_0\rangle_n = |0\rangle_1|0\rangle_2\dots\left(\frac{|0\rangle_n + |1\rangle_n}{\sqrt{2}}\right)\dots|0\rangle_{N-1}|0\rangle_N = \frac{1}{\sqrt{2}}(|\text{Vac}\rangle + |\mathbf{1}_n\rangle), \quad (5)$$

where N is the number of sites, $n \in \{1, 2, \dots, N\}$, $|\text{Vac}\rangle \equiv |0\rangle_1|0\rangle_2\dots|0\rangle_N$ is the vacuum state and $|\mathbf{1}_n\rangle = |0\rangle_1|0\rangle_2\dots|1\rangle_n\dots|0\rangle_N$ is a one-photon Fock state. The state at time t is

$$|\psi(t)\rangle_n = \frac{1}{\sqrt{2}}\left(|\text{Vac}\rangle + \sum_{\alpha} C_{\alpha,n} e^{-iE_{\alpha}^{(1)}t} |\phi_{\alpha}^{(1)}\rangle\right), \quad (6)$$

where $\alpha \in \{1, 2, \dots, N\}$, $C_{\alpha,n} = \langle\phi_{\alpha}^{(1)}|\mathbf{1}_n\rangle$ and $|\phi_{\alpha}^{(1)}\rangle$ is the one-photon eigenstate with the eigen-energy $E_{\alpha}^{(1)}$. The expectation value of $\chi_1(n) \equiv \langle\sigma_n^X\rangle + i\langle\sigma_n^Y\rangle$ takes the form

$$\chi_1(n) = \frac{1}{2} \sum_{\alpha} |C_{\alpha,n}|^2 e^{-iE_{\alpha}^{(1)}t}. \quad (7)$$

Non-vanishing peak amplitudes $|C_{\alpha,n}|^2 > 0$ can be assured by varying the initial state, i.e. varying n , to span the space of the single-photon manifold.

2.3 Two-particle spectroscopy: generalization

The initial states are product states of the form

$$|\psi_0\rangle_{n,m} = |0\rangle_1|0\rangle_2\dots\left(\frac{|0\rangle_n + |1\rangle_n}{\sqrt{2}}\right)\dots\left(\frac{|0\rangle_m + |1\rangle_m}{\sqrt{2}}\right)\dots|0\rangle_{N-1}|0\rangle_N = \frac{1}{2}(|\text{Vac}\rangle + |\mathbf{1}_n, \mathbf{1}_m\rangle) + \frac{1}{2}(|\mathbf{1}_n\rangle + |\mathbf{1}_m\rangle), \quad (8)$$

where $n \neq m$, and $m, n \in \{1, 2, \dots, N\}$ and $|\mathbf{1}_n, \mathbf{1}_m\rangle = |0\rangle_1|0\rangle_2\dots|1\rangle_n\dots|1\rangle_m\dots|0\rangle_N$ are the two-photon Fock states. The state at time t is

$$|\psi(t)\rangle_{n,m} = \frac{1}{2}\left(|\text{Vac}\rangle + \sum_{\beta} C_{\beta,(n,m)} e^{-iE_{\beta}^{(2)}t} |\phi_{\beta}^{(2)}\rangle\right) + \frac{1}{2}\left(\sum_{\alpha} (C_{\alpha,n} + C_{\alpha,m}) e^{-iE_{\alpha}^{(1)}t} |\phi_{\alpha}^{(1)}\rangle\right), \quad (9)$$

where $\beta \in \{1, 2, \dots, \frac{1}{2}N(N+1)\}$, $|\phi_{\beta}^{(2)}\rangle$ is an energy eigenstate in the two-photon manifold with the corresponding energy $E_{\beta}^{(2)}$ and $C_{\beta,(n,m)} = \langle\phi_{\beta}^{(2)}|\mathbf{1}_n, \mathbf{1}_m\rangle$. A generalized two-photon lowering operator can be constructed as

$$\chi_2(n, m) \equiv \langle\sigma_n^X \sigma_m^X\rangle - \langle\sigma_n^Y \sigma_m^Y\rangle + i\langle\sigma_n^X \sigma_m^Y\rangle + i\langle\sigma_n^Y \sigma_m^X\rangle. \quad (10)$$

This operator measures the phase difference between the vacuum and the two-photon state, while projecting out the one-photon component to avoid measuring the energy differences $E_{\beta}^{(2)} - E_{\alpha}^{(1)}$. Its expectation value takes the form

$$\chi_2(n, m) = \frac{1}{4} \sum_{\beta} |C_{\beta,(n,m)}|^2 e^{-iE_{\beta}^{(2)}t}. \quad (11)$$

One might observe that with our choice of initial states, we do not directly cover all the space in the two-photon subspace since we did not include double-occupancy states such as $|\mathbf{2}_n\rangle \equiv |0\rangle_1|0\rangle_2\dots|2\rangle_n\dots|0\rangle_N$. However, in the soft-core limit $U/J = 3.5$ where we operate, all 45 two-photon eigenstates $|\phi_{\beta}^{(2)}\rangle$ have appreciable overlap with our choice of initial states. Therefore, their energies can be measured as shown in the main text. As one get to the hardcore limit with $U/J \rightarrow \infty$, mainly 36 out of 45 eigen-energies will be picked up by $\chi_2(n, m)$, which again are all the physically relevant ones to probe the physics of the system in this regime.

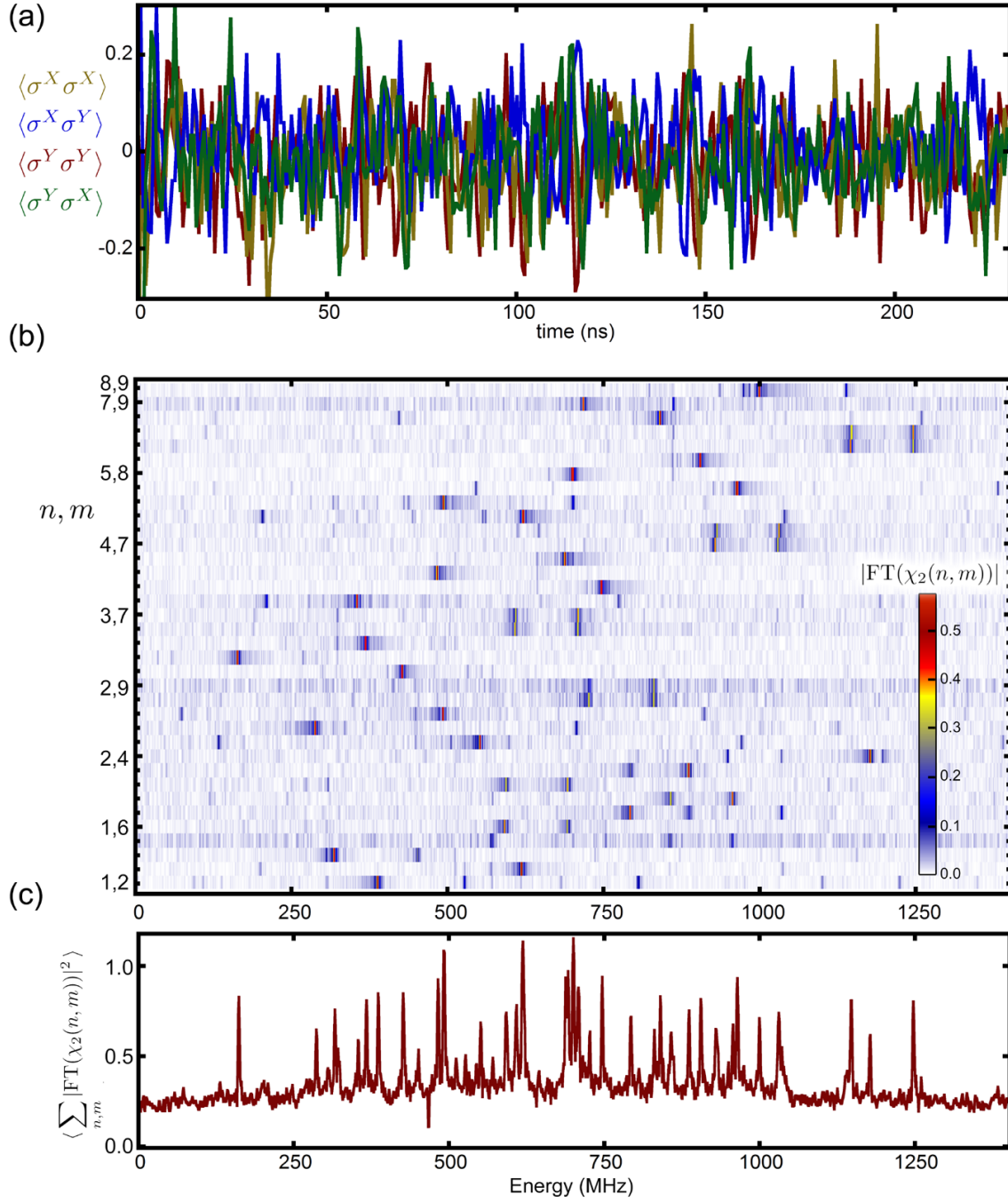


Figure S3. **Spectroscopy of energy levels in the two-photon manifold** The protocol for taking data in the two-photon manifold is very similar to the method illustrated in Fig. (1) of the main text. (a) A typical time-domain measurement of the two-point correlations that are needed for constructing $\chi_2(n, m)$. For this data set $n = 5$ and $m = 7$. Similar measurements are done for every $m, n \in \{1, 2, \dots, N\}$ with $n \neq m$. (b) The magnitude of the Fourier transform of $\chi_2(n, m)$ for all m and n choices with $m, n \in \{1, 2, \dots, N\}$ and $n \neq m$. (c) Average of Fourier transforms presented in (b).

2.4 Computation of the Participation Ratio

Here, we discuss in details how the participation ratios in the two-photon manifold are measured and computed. In the Bose-Hubbard Hamiltonian

$$H_{BH} = \sum_{n=1}^9 \mu_n a_n^\dagger a_n + \frac{U}{2} \sum_{n=1}^9 a_n^\dagger a_n (a_n^\dagger a_n - 1) + J \sum_{n=1}^8 a_{n+1}^\dagger a_n + a_n^\dagger a_{n+1}, \quad (12)$$

we set $J/2\pi = 50$ MHz. By design of the chip, U is fixed $U/2\pi = 175$ MHz. We realize a quasi-periodic potential by setting $\mu_n = \Delta \cos(2\pi nb)$, where $b = (\sqrt{5} - 1)/2$. We vary Δ from 0 to $\Delta/2\pi = 300$ MHz. Choosing the inverse of the so-called golden ratio for b stems from the fact that this irrational number is considered to be "very" irrational number, meaning that approximating it in terms of ratio of integers involves large numbers. Nevertheless, in setting the parameters in the lab, there is no meaningful distinction between rational and irrational numbers. We chose this number just to reduce the chance of commensurability with the lattice, which could have been the case if we chose a number close to 0.5 or 0.33.

Initial states are made by placing two qubits (Q_n and Q_m) in the superposition of the $|0\rangle$ and $|1\rangle$ state. We measure two-point correlations and construct $\chi_2(n, m) \equiv \langle \sigma_n^X \sigma_m^X \rangle - \langle \sigma_n^Y \sigma_m^Y \rangle + i \langle \sigma_n^X \sigma_m^Y \rangle + i \langle \sigma_n^Y \sigma_m^X \rangle$. We consider all pairs of qubits for the initial states $n, m \in \{1, 2, \dots, 9\}$. In the two-photon energy manifold, there are 36 single (e.g. $|\mathbf{1}_3, \mathbf{1}_7\rangle = |001000100\rangle$) and 9 double occupancy states (e.g. $|\mathbf{2}_5\rangle = |000020000\rangle$), which gives $\binom{9}{2} + \binom{9}{1} = 45$ energy levels. In the two-photon energy manifold of Eqn. (2), we create all 36 single-occupation initial states:

$$|\psi_0\rangle_{n,m} \equiv |0\rangle_1 |0\rangle_2 \dots \left(\frac{|0\rangle_n + |1\rangle_n}{\sqrt{2}} \right) \dots \left(\frac{|0\rangle_m + |1\rangle_m}{\sqrt{2}} \right) \dots |0\rangle_{N-1} |0\rangle_N \quad (13)$$

In the average of the magnitude of FT of data (summed over all these 36 initial states), we identify 45 peaks. This constitute $\{E_\alpha\}$, a set of 45 eigen-energies of the Hamiltonian. Note that the number of initial states that one can begin with is technically infinitely many. Using more initial states only adds to the confidence for the detected peaks. Since all the eigen-energies of the Hamiltonian has been identified, by choosing one of the initial states, (e.g. $|001000100\rangle$), we can see how extended it is in the energy landscape. This is done by considering the FT of the data and reading the magnitude of FT for all E_α values. Therefore in the expansion

$$|\psi_0\rangle_{n,m} = \sum_{\alpha} C_{\alpha,(n,m)} |\phi_{\alpha}\rangle \quad (14)$$

we now know $\{P_{\alpha,(n,m)}\} = \{|C_{\alpha,(n,m)}|^2\}$. Next, we want to extract the expansion of Fock states $|1_n\rangle$ from the expansions of our initial states that involved two photons. This is simply done by adding probabilities of the initial states which share one of the excited qubits $P_{\alpha,n} = \sum_m P_{\alpha,(n,m)}$. Now we can compute

$$PR_{\text{Energy}}(n) \equiv \frac{1}{\sum_{\alpha} P_{\alpha,n}^2}, \quad (15)$$

which is a measure of the spread of a real-space localized state in energy landscape. Note that since $\sum_{\alpha} P_{\alpha,n} = 1$, the PR_{Energy} is the simplest non-trivial moment of the probability distribution, which tells us about the spread of wavefunctions. The expansion of energy eigenstate in real space $|\phi_{\alpha}\rangle = \sum_n C_{\alpha,n} |\mathbf{1}_n\rangle$ is readily done by summing over n

$$PR_{\text{space}}(\alpha) \equiv \frac{1}{\sum_n P_{\alpha,n}^2}. \quad (16)$$

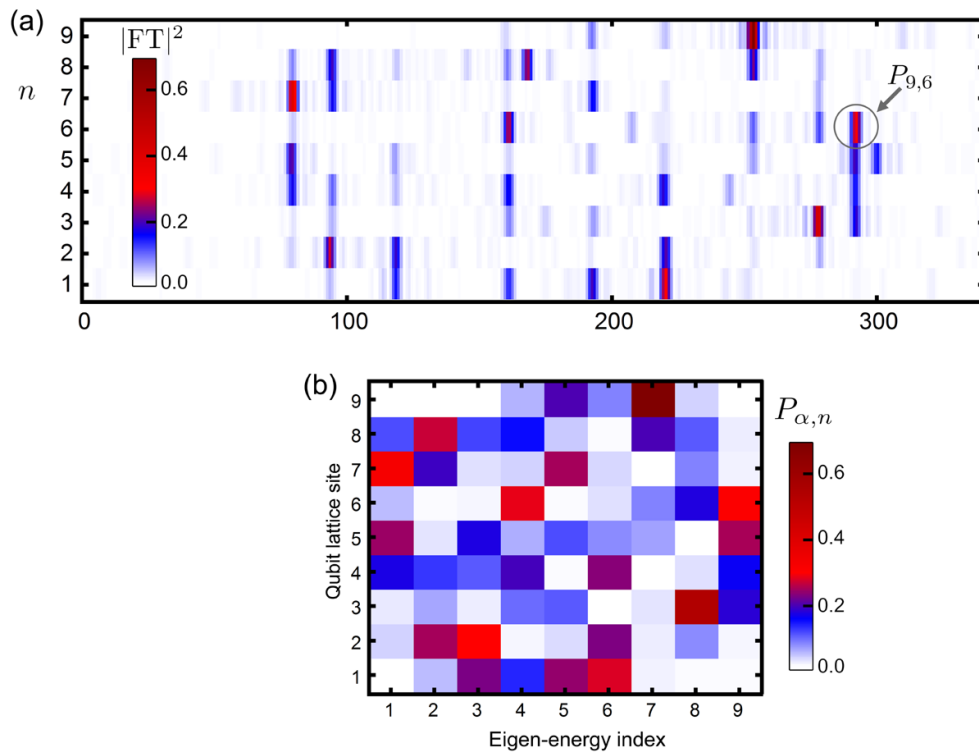


Figure S4. **Computation of the Participation Ratio in the single-photon manifold.** (a) This is the same plot as Fig.1 (c) of the main text and for the ease of comparison is represented in here. (b) After identification of the peaks, we ask what is the magnitude of FT (false color) at each site (vertical axis) for a given eigen-energy (horizontal axis). We normalize the amplitudes such that $\sum_n P_{\alpha,n} = 1$ and $\sum_{\alpha} P_{\alpha,n} = 1$.

2.5 Resolving the spectrum for large Hilbert-spaces

In this section, we address the main technical challenge that arises when dealing with a large many-body system. What sets the limit on how small and large energy differences we can resolve?

In the current work the main limitation comes from the data collecting rate. Each panel in the two-photon manifold (Fig 3,4, and 5), where we change Δ in about 20 steps, took about 2 days to be collected. Recall that we generated all single-occupancy two-photon states for every realization of the Hamiltonian. This is not a fundamental limit and one can take data for longer time, but we impose this limit ourselves. Instead of taking data with this rate for a longer time, we are addressing the core of this issue and working on improving our data taking rate. There are indications that with fast resetting techniques and better data streaming, we can improve the data taking rate by two orders of magnitude. These ideas will be tested and implemented in the future generations of our devices. These methods would help to push the limitations for implementation of our spectroscopy method to be limited only by the coherent time of the system.

When the system size N is increased, missing some energy peaks in the measurement will eventually become unavoidable because the resolution in the energy Fourier spectrum is fixed by the coherence time of the system. Here, we analyze what happens to level statistics when some levels are missing. To study the deviation from the ideal level spacing distributions, we use the Kullback-Leibler divergence and estimate the efficiency of our method

$$D_{KL}(P||Q) = \sum_l P(r_l) \log \left(\frac{P(r_l)}{Q(r_l)} \right). \quad (17)$$

The KL divergence is close to zero when the two distributions P and Q are close. In Fig.S5(a) we show the number of missing levels for different parameter regimes and a fixed resolution of $1MHz$. Even for a finite size $N = 18$, it is interesting that one misses more levels close to the critical point of the AA model $\Delta \approx 2J$. This is expected because close to the critical point, some levels cluster and the statistics is neither Poisson nor GOE. Therefore, for a finite resolution of the Fourier spectrum, there would be more missing levels. Fig.S5(b) shows a second step to test the efficiency of our method. We calculate numerically the KL divergence for a fixed resolution which leads to different number of missing levels for different parameters.

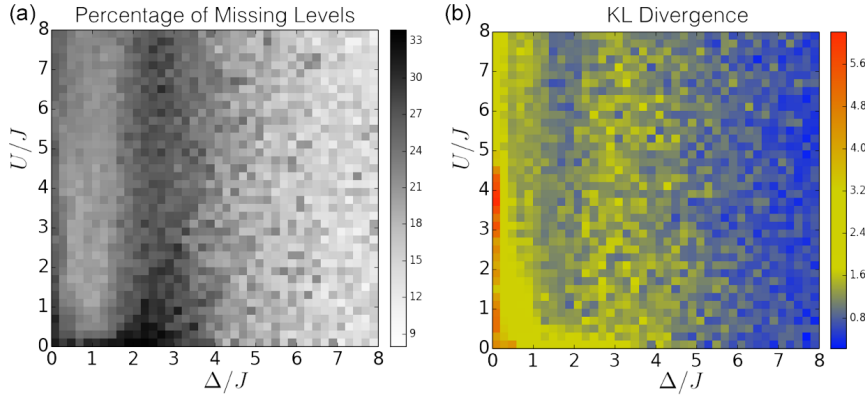


Figure S5. **The effect of missing levels in level statistics** We numerically simulate a system of two interacting particles in a lattice with $N = 18$ sites and $J/2\pi = 50\text{MHz}$. **(a)** For a fixed resolution of 1MHz , we calculate the percentage of missing levels for different parameter regimes. **(b)** To determine the effect of missing levels on the statistics we use the Kullback-Leibler (KL) divergence between the measured distribution (which had missing levels) to the distribution without missing levels.

3. TWO-POINT QUANTUM CORRELATIONS

Here we discuss the details of the two-point correlation measurements and also provide the numerical simulations. In the Bose-Hubbard Hamiltonian

$$H_{BH} = \sum_{n=1}^9 \mu_n a_n^\dagger a_n + \frac{U}{2} \sum_{n=1}^9 a_n^\dagger a_n (a_n^\dagger a_n - 1) + J \sum_{n=1}^8 a_{n+1}^\dagger a_n + a_n^\dagger a_{n+1}, \quad (18)$$

we set $J/2\pi = 50\text{MHz}$. By design of the chip, U is fixed $U/2\pi = 175\text{MHz}$. We realize a quasi-periodic potential by setting $\mu_n = \Delta \cos(2\pi nb)$, where $b = (\sqrt{5} - 1)/2$, and vary Δ .

In the data presented in Fig. (5) of the main text, The initial states are made by placing two qubits (Q_n and Q_m) in the superposition of the $|0\rangle$ and $|1\rangle$ states. We measure $\mathcal{S}_{m,n} = |\langle \sigma_m^1 \sigma_n^2 \rangle - \langle \sigma_m^1 \rangle \langle \sigma_n^2 \rangle|$, where $\sigma^1, \sigma^2 \in \{\sigma^X, \sigma^Y\}$ and $m, n \in \{1, 2, \dots, 9\}$, for all m and n combinations and choices of Pauli operators. The number of pairs of qubits that one can pick for exciting initially and measuring the two-point correlation is $\binom{9}{2} = 36$. The total number of choices for Pauli operators is 4 (XX, YY, XY, YX), which means that $36 \times 4 = 144$ distinct $\mathcal{S}_{m,n}$ are measured. Next, we average $\mathcal{S}_{m,n}$ over time, from 0 to 250 ns, and over the 4 choices of the Pauli operators, and over all qubit pair combinations with the same $|m - n|$. This gives $\tilde{\mathcal{S}}_{m,n}$ for a given realization of Hamiltonian (a given Δ/J) as a function of $|m - n|$.

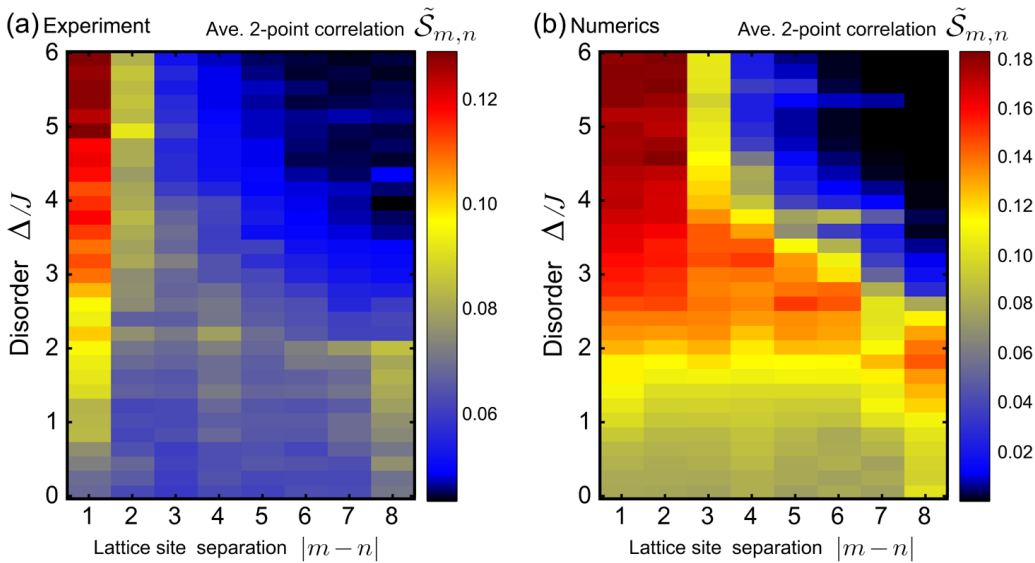


Figure S6. **Numerical calculation of the quantum correlations** We consider $J/2\pi = 50\text{MHz}$, which fixes the interaction $U/J = 3.5$. The time-averaged (from 0 to 250 ns) correlation $\mathcal{S}_{m,n} = |\langle \sigma_m^1 \sigma_n^2 \rangle - \langle \sigma_m^1 \rangle \langle \sigma_n^2 \rangle|$ for $b = (\sqrt{5} - 1)/2$ and a system size $N = 9$ is **(a)** experimentally measured (same as Fig. 5 in the manuscript), and **(b)** numerically computed.

4. HAMILTONIANS USED IN THIS WORK

4.1 Mapping the 2D quantum Hall model to the 1D Harper model

An electron moving in a 2D lattice with a perpendicular magnetic field b is described by the quantum Hall model,

$$H_{IQH} = J_x \sum_{n,m} (\hat{a}_{n,m}^\dagger \hat{a}_{n+1,m} + H.c.) + J_y \sum_{n,m} (\hat{a}_{n,m}^\dagger \hat{a}_{n,m+1} e^{2\pi b n} + H.c.) \quad (19)$$

where J_x and J_y are hopping strength along x and y axes respectively, see Fig.S7. For a periodic boundary condition on the y-direction, one can define the quantum Fourier transform $\hat{a}_{n,m}^\dagger = \sum_k e^{-ikm} \hat{a}_{n,k}^\dagger$. Substituting this to Eq.19, we get $H_{IQH} = \sum_k H_k$, where

$$H_k = 2J_y \sum_n \cos(2\pi b n + k) \hat{a}_{n,k}^\dagger \hat{a}_{n,k} + J_x \sum_n (\hat{a}_{n,k}^\dagger \hat{a}_{n+1,k} + H.c.) \quad (20)$$

The 1D harper model is then achieved by dropping the index k in $\hat{a}_{n,k}$ and replacing $2J_y$ and J_x with Δ and J , respectively. We set $k = 0$ in the main text. Edge states in the Harper model has been studied in [5].

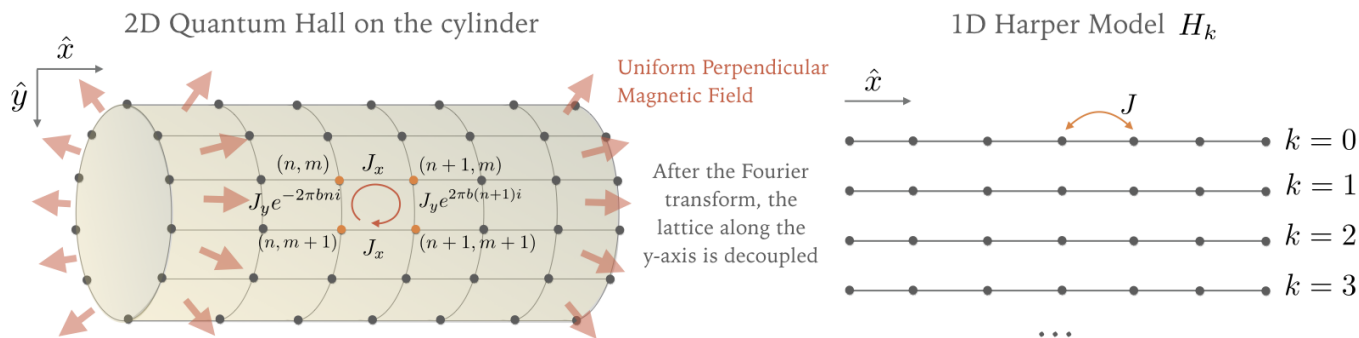


Figure S7. Illustration of the 2D Quantum Hall model and its mapping to the 1D Harper model.

4.2 Aubry-Andre model

In the absence of interactions (or at single-particle level), the Eqn. 3 of the main text is the celebrated Aubry-Andre (AA) model[6, 7]. We compare this model with the well-studied Anderson model. In 1D or 2D Anderson model, any amount of disorder would localize the entire system and there is no phase transition, or transition is at zero disorder. However, in the 3D Anderson model there is a localization-delocalization transition, where a mobility edge appears [8]. Similar to the 3D Anderson model, the 1D AA model exhibits a localization-delocalization transition. In the AA model, when $\Delta = 2J$, all the eigenstates are fully localized (delocalized) for $\Delta > 2J$ ($\Delta < 2J$) and the localization length is independent of the energy and is solely determined by the ratio between Δ and J [7]. Therefore, the AA model does not exhibit mobility edge [9]. The main difference between the 3D Anderson model and the AA model is that in the AA model, the delocalized phase is characterized by ballistic transport, i.e., scattering events are rare[6]. This implies a ballistic spreading of an initial state localized at a given site.

Now let us discuss briefly the effect of interactions in the AA model (Eqn.2 of the main text) and a discussion about the signatures of the mobility edge. In the interacting case, one can use the basis of single-particles states of the AA model and in this representation, the interaction act as a hopping term in energy space, allowing transitions between different single-particle states [7]. In systems with a single-particle mobility edge, like 3D Anderson model, the interaction couples localized and delocalized states[9]. This happens because for a given strength of disorder, localized and delocalized states coexist. In the case of the AA model, as there is not mobility edge in the noninteracting case, the interaction just couples single-particle states which are either localized or delocalized. The signatures of the mobility edge observed in the experiment can be explained as a consequence of the interaction between the two particles in the lattice. When they are located at a distance smaller that the single-particle localization length, they form a bound state that spreads ballistically, as it has been reported in the literature [10]. When the particles are far apart, i.e., at a distance longer than the localization length, they remain localized. This argument explain the coexistence of localized

and delocalized states in the interacting model for a fixed disorder and provides an explanation for the signatures of the mobility edge seen in Fig. (3).

* These authors contributed equally to this work.

† jmartinis@google.com

- [1] Yu Chen, C. Neill, P. Roushan, N. Leung, M. Fang, R. Barends, J. Kelly, B. Campbell, Z. Chen, B. Chiaro, A. Dunsworth, E. Jeffrey, A. Megrant, J. Mutus, C. Quintana, D. Sank, A. Vainsencher, J. Wenner, C. White, T., Michael R. Geller, A. Cleland, and John M. Martinis, “Qubit architecture with high coherence and fast tunable coupling,” *Phys. Rev. Lett.* **113**, 220502 (2014).
- [2] M. Geller, E. Donate, Y. Chen, Michael T. Fang, N. Leung, C. Neill, P. Roushan, and J. Martinis, “Tunable coupler for superconducting xmon qubits: Perturbative nonlinear model,” *Phys. Rev. A* **92**, 012320 (2015).
- [3] C. Neill, P. Roushan, M. Fang, Yu Chen, R. Kolodrubetz, M. and Barends, J. Kelly, B. Campbell, Z. Chen, B. Chiaro, A. Dunsworth, E. Jeffrey, A. Megrant, Y. Mutus, J., J. J. O’Malley, P., M. Quintana, C., D. Sank, A. Vainsencher, J. Wenner, C. White, T., A. A. Polkovnikov, and J. Martinis, “Ergodic dynamics and the resulting thermalization in an isolated quantum system,” under review (2015).
- [4] C. Neill, “Thesis, under preparation,” (2017).
- [5] Yaacov E. Kraus, Yoav Lahini, Zohar Ringel, Mor Verbin, and Oded Zilberberg, “Topological states and adiabatic pumping in quasicrystals,” *Phys. Rev. Lett.* **109**, 106402 (2012).
- [6] Shankar Iyer, Vadim Oganesyan, Gil Refael, and David A. Huse, “Many-body localization in a quasiperiodic system,” *Phys. Rev. B* **87**, 134202 (2013).
- [7] V. P. Michal, B. L. Altshuler, and G. V. Shlyapnikov, “Delocalization of weakly interacting bosons in a 1d quasiperiodic potential,” *Phys. Rev. Lett.* **113**, 045304 (2014).
- [8] E. Abrahams, P. W. Anderson, D. C. Licciardello, and T. V. Ramakrishnan, “Scaling theory of localization: Absence of quantum diffusion in two dimensions,” *Phys. Rev. Lett.* **42**, 673–676 (1979).
- [9] Xiaopeng Li, Sriram Ganeshan, J. H. Pixley, and S. Das Sarma, “Many-body localization and quantum nonergodicity in a model with a single-particle mobility edge,” *Phys. Rev. Lett.* **115**, 186601 (2015).
- [10] Sergej Flach, Mikhail Ivanchenko, and Ramaz Khomeriki, “Correlated metallic two-particle bound states in quasiperiodic chains,” *EPL (Europhysics Letters)* **98**, 66002 (2012).